



Silica/titania composite-supported Ni catalysts for CO methanation: Effects of Ti species on the activity, anti-sintering, and anti-coking properties



Jun Ren ^{*}, Haidong Li, Yongyong Jin, Jiyu Zhu, Shusen Liu, Jianying Lin, Zhong Li

Key Laboratory of Coal Science and Technology (Taiyuan University of Technology), Ministry of Education and Shanxi Province, Taiyuan 030024, China

ARTICLE INFO

Article history:

Received 7 June 2016

Received in revised form 11 August 2016

Accepted 28 August 2016

Available online 29 August 2016

Keywords:

Composite oxides

Ni catalysts

Support effect

Electron effect

CO methanation

ABSTRACT

Catalysts composed of Ni supported on $\text{SiO}_2/\text{TiO}_2$ composite oxides (ST) with different Si/Ti molar ratios have been prepared by an ultrasonic impregnation method and used in CO methanation. Experimental results show that the ST systems have large specific surface area, large pore volume, and offer suitable metal–support interactions, thereby facilitating the dispersion of Ni. Indeed, these catalysts have more suitable Ni active sites for methanation, and the composite oxides show good support and synergistic effects. Thus, Ni/ST_x ($x = 50, 10, 5, 1$) with a Ni loading of 10 wt% displayed higher catalytic performances relative to catalysts composed of Ni supported on individual oxides (SiO_2 , TiO_2 , and $\gamma\text{-Al}_2\text{O}_3$). Among the catalysts, $10\text{Ni}/\text{ST}5$ displayed the best catalytic activity (370 °C, CO conversion: 99.9%, CH_4 selectivity: 95.6%). Furthermore, $10\text{Ni}/\text{ST}5$ showed better CH_4 yield (290 °C, CH_4 yield: 92.4%), anti-sintering properties (smaller Ni particles), and anti-coking properties (lower amount of deposited carbon) after a stability test of duration 144 h at 600 °C than those of a typical $10\text{Ni}/\gamma\text{-Al}_2\text{O}_3$ catalyst (290 °C, CH_4 yield: 80.0%). This can be attributed to the optimal amount of TiO_2 separating/separated from the ST5 and playing the role of an electronic promoter. It not only effectively facilitated the dispersion of Ni during sintering, but also triggered electron transfer and enhanced the electron cloud density of Ni^{00} ($\text{Ni}^{00} \rightarrow \text{Ni}^{\delta-}$), thereby weakening the C–O bond of Ni–C–O and enhancing the dissociation of CO.

© 2016 Elsevier B.V. All rights reserved.

1. Introduction

With the consumption of fossil fuels and pollutant emissions, there is an urgent need to seek and develop clean, environment friendly, and sustainable energy sources. Methane (CH_4), the primary component of natural gas, has been considered as an efficient energy carrier because of its clean nature, high calorific value, and high energy efficiency. However, in recent years, in view of the increasing demand for natural gas and the rise in its cost, some countries have introduced countermeasures to address the issue of dwindling supplies. Among them, the production of synthetic or substitute natural gas (SNG) via syngas from coal or biomass or of coke oven gas (COG) by methanation reaction are effective methods. Especially in China, coal-to-SNG has attracted particular attention due to the “deficient oil, lean gas, rich coal” energy structure. Methanation reactions, including CO and CO_2 methanations, are key processes in SNG production. The application of CO_2

methanation can produce energy fuels and reduce the greenhouse gas effect. In addition, over the past years, CO methanation has been well developed and widely used in the chemical industry, including the removal of trace amounts of CO (ca. 1 vol%) from H_2 -rich feed gas, and gas purification for the NH_3 synthesis process and fuel cells, as well as processes relating to Fischer–Tropsch synthesis. However, catalysts used for methanation of high CO concentrations are not only easily poisoned, but also rapidly deactivate at high temperatures due to sintering and carbon deposition. Thus, it is necessary to develop a highly efficient methanation catalyst with superior thermal stability as well as anti-sintering and anti-coking properties.

Since Sabatier and Senderens first discovered the methanation reaction in 1902, a series of methanation catalysts have been extensively investigated by researchers. The group VIII metals (such as Ru [1,2], Rh [3], Fe [4], Ni [5], Pd [6] and so on) have been investigated and used in methanation reactions as the key active components of the catalysts. From Mills and Steffgen's research on methanation [7], it can be concluded that the activity order of various metals in methanation reactions is Ru > Ir > Rh > Ni > Co > Os > Pt > Fe > Mo > Pd > Ag. Among systems

^{*} Corresponding author at: No. 79 Yingze West Street, Taiyuan 030024, China.
E-mail addresses: renjun@tyut.edu.cn, 286945754@qq.com (J. Ren).

involving these metals, Ru-based catalysts are considered to be the most active for methanation, but the scarcity and expense of noble Ru restrict their large-scale application. Nickel-based catalysts for methanation have been recognized as the most appropriate because of their relatively high activity, selectivity, and low cost. On the other hand, there have been extensive studies of catalyst supports such as Al_2O_3 [8–10], SiO_2 [11,12], TiO_2 [13–15], CeO_2 [16], ZrO_2 [17], silicon molecular sieves [18], and so on. Takenaka et al. [19] demonstrated that the CO methanation performances of Ni-based catalysts are closely related to the nature of the support used; they found that CO conversions at 250 °C increased in the order $\text{Ni/MgO} < \text{Ni/Al}_2\text{O}_3 < \text{Ni/SiO}_2 < \text{Ni/TiO}_2 < \text{Ni/ZrO}_2$. In addition, based on the technological processes of methanation in the chemical industry, Schildhauer [20] comprehensively reviewed SNG production from coal and dry biomass in the period from 1950 to 2009. Titanium dioxide (TiO_2)-supported Ni catalysts have exhibited good catalytic performance in low-concentration methanation at low temperatures [21]. However, TiO_2 as a catalyst support showed low activity in high-temperature methanation due to its poor thermal and mechanical stability. Zeng et al. [22] reported the preparation of $\text{Ni}/\gamma\text{-Al}_2\text{O}_3$ catalysts modified with TiO_2 by a solution combustion method and their application for CO methanation. The results showed that Ti species served as a promoter, suppressing the formation of NiAl_2O_4 , enhancing the utilization of Ni species, and increasing the CO adsorption capacity, thereby improving the catalytic performance. In addition, SiO_2 -supported Ni catalysts for high-concentration and high-temperature methanation are considered to show relatively low activity compared to Al_2O_3 -supported Ni catalysts. This is due to the weak metal–support interaction between Ni and SiO_2 [23], which can lead to Ni sintering and aggregation. As a result, the Ni is poorly dispersed on the support. Nevertheless, a combination of these two oxides as a catalyst support could have high thermal stability and provide suitable metal–support interaction, improving the catalytic performance.

In the present work, mesoporous $\text{SiO}_2/\text{TiO}_2$ composite supports with high specific surface area have been successfully prepared by a sol–gel method without a template, which shows higher thermal stability and provides more suitable metal–support interactions relative to both SiO_2 and TiO_2 , making them potentially useful as supports in CO methanation. Their features of high specific surface area and pore size can be achieved by adjusting the Si/Ti atomic ratio and controlling the temperature and duration of the calcination process. A series of $10\text{Ni}/\text{STx}$ ($x = \text{Si/Ti}$ atomic ratio) catalysts have been prepared by an ultrasonic co-impregnation method. The effects of the physical, chemical, and textural features of the composite supports as well as coke formation in CO methanation have been studied. The origin of the high performance of the catalysts is speculated upon.

2. Experimental

2.1. Materials

All reagents mentioned in this paper, i.e., tetraethyl orthosilicate (TEOS) as silicon source of the composite oxides precursors, titanium tetraisopropoxide (TTIP) as titanium source of the precursors, ethyl alcohol (EtOH), acetic acid (HAc), nickel(II) nitrate hexahydrate ($\text{Ni}(\text{NO}_3)_2 \cdot 6\text{H}_2\text{O}$), and these reagents were purchased from Sinopharm Chemical Reagent Co. and were of AR grade. $\gamma\text{-Al}_2\text{O}_3$ (99% purity, Sinopharm Chemical Reagent Co.) as the individual oxide support was used for comparison to the composite oxides in CO methanation.

2.2. Catalyst preparation

2.2.1. Synthesis of the $\text{SiO}_2/\text{TiO}_2$ composites

Mesoporous ST composite supports with high specific surface area were prepared by a co-gelation method without a template according to our previous study [24]. The preparation process was as follows: two different solutions consisting of (A) $\text{V}(\text{EtOH})/\text{V}(\text{TEOS})/\text{V}(\text{HAc})/\text{V}(\text{H}_2\text{O}) = 8:4:2:1$ and (B) $\text{V}(\text{EtOH})/\text{V}(\text{TTIP})/\text{V}(\text{HAc})/\text{V}(\text{H}_2\text{O}) = 8:4:2:1$ were placed in two separate beakers. Solution A was slowly poured into solution B to form the mixed system C. The mouth of the beaker containing mixed system C was covered with the preservative film and the contents were continuously stirred until they converted into a solid co-gel. The co-gel was set aside at room temperature for about 1 week to eliminate solvents (such as alcohols and water), and the xerogel precursor was obtained. Then the xerogel precursor was heated in a muffle furnace at a rate of 0.5 °C/min from room temperature to 65 °C and held for 3 h; next it was further heated to 550 °C at the same rate for another 4 h to eliminate the organic residues. Finally, a white $\text{SiO}_2/\text{TiO}_2$ composite was thereby obtained, which was designated as STx (where x denotes the Si/Ti atomic ratio). In addition, the $\text{SiO}_2/\text{TiO}_2$ composite oxides with various components were achieved by adjusting the Si/Ti atomic ratio.

2.2.2. Preparation of the catalysts

The catalysts were prepared by an ultrasonic impregnation method. Firstly, a specified amount of nickel(II) nitrate hexahydrate ($\text{Ni}(\text{NO}_3)_2 \cdot 6\text{H}_2\text{O}$) was ultrasonically dissolved in deionized water under vigorous stirring at 65 °C for 20 min. The support powder (STx , $\gamma\text{-Al}_2\text{O}_3$) was slowly added to the nickel nitrate aqueous solution to form a mixture. Next, the mixture was ultrasonicated and stirred for 1 h at 65 °C to ensure good dispersion and then it was further stirred continuously at constant temperature until the solvent was almost removed. Finally, these obtained samples were dried at 80 °C overnight in an oven and then calcined at 500 °C for 2 h in a muffle furnace to obtain catalysts. These obtained catalysts are labelled as $10\text{Ni}/\text{STx}$ ($10\text{Ni}/\gamma\text{-Al}_2\text{O}_3$), where 10 represents the weight content of Ni species.

2.3. Catalyst evaluation

The catalytic tests of the catalysts for CO methanation were investigated in a fixed-bed microreactor instrument (length: 40 cm, inner diameter: 1 cm) equipped with the quartz lining tube, in order to eliminate the effects of stainless steel reactor to the deposited carbon species for the catalysts. 0.4 g fresh catalyst sample with 40–60 mesh particle sizes was used for each evaluation process. Firstly, the catalysts were reduced at 550 °C for 2 h by pure hydrogen with a flow rate of 30 mL min^{-1} before reaction; afterwards, the temperature was cooled down from 550 °C to 190 °C. Next, the 100 mL min^{-1} of reaction gases with $\text{V}(\text{H}_2)/\text{V}(\text{CO}) = 3:1$ were introduced into the microreactor instrument. The reactions were performed under the weight hourly space velocity (WHSV) of $15000 \text{ mL g}^{-1} \text{ h}^{-1}$ at 1.0 MPa in the temperature range of 190–450 °C. In addition, the long-term stability test with 144 h of the catalyst was examined; in each test, 0.2 g fresh catalyst was used, and the reaction was performed under a WHSV of $30000 \text{ mL g}^{-1} \text{ h}^{-1}$ and 1.0 MPa at 500 °C and 600 °C. The reaction products were analyzed on line through a GC900SD gas chromatograph equipped with a TDX-01 column and a thermal conductivity detector (TCD). The formulas for CO conversion, CH_4 selectivity, CH_4 yield, and turnover frequency of CO methanation were calculated based on Eqs. (1)–(4) as follows:

CO conversion (X_{CO} , %):

$$X_{CO} = \frac{F_{CO,in} - F_{CO,out}}{F_{CO,in}} \times 100\% \quad (1)$$

CH₄ selectivity (S_{CH_4} , %):

$$S_{CH_4} = \frac{F_{CH_4,out}}{F_{CO,in} - F_{CO,out}} \times 100\% \quad (2)$$

CH₄ yield (Y_{CH_4} , %):

$$Y_{CH_4} = \frac{X_{CO} \times S_{CH_4}}{100} = \frac{F_{CH_4,out}}{F_{CO,in}} \times 100\% \quad (3)$$

TOF of CO conversion:

$$TOF_{CO} (s^{-1}) = \frac{X_{CO} \times F_{CO,in} \times NA}{V_g \times A} \quad (4)$$

where, $F_{i,in}$ and $F_{i,out}$ represent respectively the volume flow rate of i ($i = CO$ or CH_4) species at the gas inlet and outlet of reactor (mL min^{-1}); NA is the avogadro's constant ($6.02 \times 10^{23} \text{ mol}^{-1}$); V_g is the molar volume of gas at standard temperature and pressure ($22414 \text{ mL mol}^{-1}$); A represents the number of the Ni surface active sites.

2.4. Catalyst characterization

The analysis of crystal structure and phase composition of the catalyst was detected by the X-ray diffraction (XRD) characterization on a Rigaku D/Max 2500 system with a Cu K α radiation ($\lambda = 1.54056 \text{ \AA}$) and graphite monochromator. The voltage and current of the measurements were operated at 40 kV and 100 mA, and the scanning speed was $4^\circ/\text{min}$ at the scanning region of $5\text{--}85^\circ$. The crystallite size of metal Ni for the catalysts was calculated by using the Scherrer equation.

The specific surface area and pore size distribution of the samples by the N₂ adsorption–desorption characterization were investigated at -196°C on a Micromeritics 3H-2000PS2 (BeiShiDe Instruments S&T, (Beijing) Co., Ltd) specific surface area and pore size analysis instrument. Prior to the measurement, the samples were pretreated by degassing at 300°C under vacuum for 3 h. The specific surface areas of the samples were calculated by Brunauer–Emmett–Teller (BET) method and the pore volume and pore size distribution of the samples by Barrett–Joyner–Halenda (BJH) method.

The microscopic features such as the surface morphology and dispersion of active components of samples were observed using transmission electron microscopy (TEM) (JEM-2010F, JEOL, Japan). The samples were adequately dispersed in absolute ethyl alcohol through ultrasonic method; after a period time, the samples can be made by dripping the upper solution to the brass or micro grid.

The H₂ temperature-programmed reduction (H₂-TPR) measurements of the samples were performed on a Micromeritics AutoChem II 2920 analyzer. 50 mg of sample was used for each test. Firstly, 20 mL min^{-1} of Ar was introduced at 300°C for 30 min to remove adsorbed H₂O and other volatile gases on the surface of the sample for the sake of avoiding the interference of signal detection. Next, the sample was cooled to room temperature, and the gas was then switched to a 10 vol% H₂–90% Ar mixture at a flow rate of 20 mL min^{-1} . Finally, the temperature at a heating rate of $10^\circ\text{C min}^{-1}$ was elevated to 900°C .

H₂ temperature-programmed desorption (H₂-TPD) measurements of the samples were analyzed on the same instrument that was used in the H₂-TPR measurements. Before measurements, firstly, the catalysts were reduced by H₂, and then 10 vol% H₂–90% Ar mixture gas at a flow rate of 20 mL min^{-1} was introduced at room temperature for 30 min. Next, the H₂ desorption curves were

obtained at a rate of $10^\circ\text{C min}^{-1}$ from room temperature to 860°C . The desorbed H₂ was detected by using a TCD.

The number of surface active Ni sites per unit mass of the catalyst was calculated according to the results of H₂ pulse adsorption and all through it is assumed that H/Ni adsorption stoichiometry was 1:1.

The Ni dispersion (D_{Ni}) of the catalyst was calculated from Eq. (5):

$$D_{Ni} = \frac{2 \times V_{ad} \times M \times SF}{m \times P \times V_m \times d_r} \times 100 \quad (5)$$

where, V_{ad} represents the absorbed H₂ volume based on the results of H₂ pulse at standard temperature and pressure (STP) (mL); M : the molecular weight of Ni (58.69 g mol^{-1}); SF: the stoichiometric factor, which is taken as 1; m : the sample weight; P : the Ni weight percentage in the sample; V_m : the gas molar volume at STP ($22.414 \text{ L mol}^{-1}$); and d_r : the nickel species reduction ratio by the H₂-TPR profile (%).

The Ni K-edge X-ray absorption fine structure (XAFS) analysis of the catalysts was performed by the Soft X-ray Micro-characterization Beamline (SXRMB) of the Canadian Light Source (CLS). SXRMB is a medium energy with the range of 1.7–10 keV. The monochromator of the beamline consists of two pairs of crystals, which are InSbC (111) and Si (111).

O₂ temperature-programmed oxidation (O₂-TPO) experiments of the samples were carried out on a Micromeritics AutoChem II 2920 instrument. Firstly, the sample was purged by pure He with a flow rate of 20 mL min^{-1} at 300°C for 30 min, in order to eliminate the adsorbed H₂O and other volatile gases. Next, the temperature was cooled down to room temperature; and the sample was exposed to a 20 mL min^{-1} mixture gas with 5 vol% O₂–95% He. Finally, the temperature of the reactor was heated from room temperature to 900°C at a rate of $10^\circ\text{C min}^{-1}$.

The Raman spectra for the sample catalysts was conducted on a Renishaw in Via microlaser Raman spectrometer with a 514.5 nm wavelength Ar⁺ laser, and the region range was $800\text{--}2000 \text{ cm}^{-1}$ at a 1 cm^{-1} step length.

The Ni content in the catalysts was measured by inductive coupled plasma (ICP) analysis on the device Thermo iCAP6300.

3. Results and discussion

3.1. Characterization of catalysts

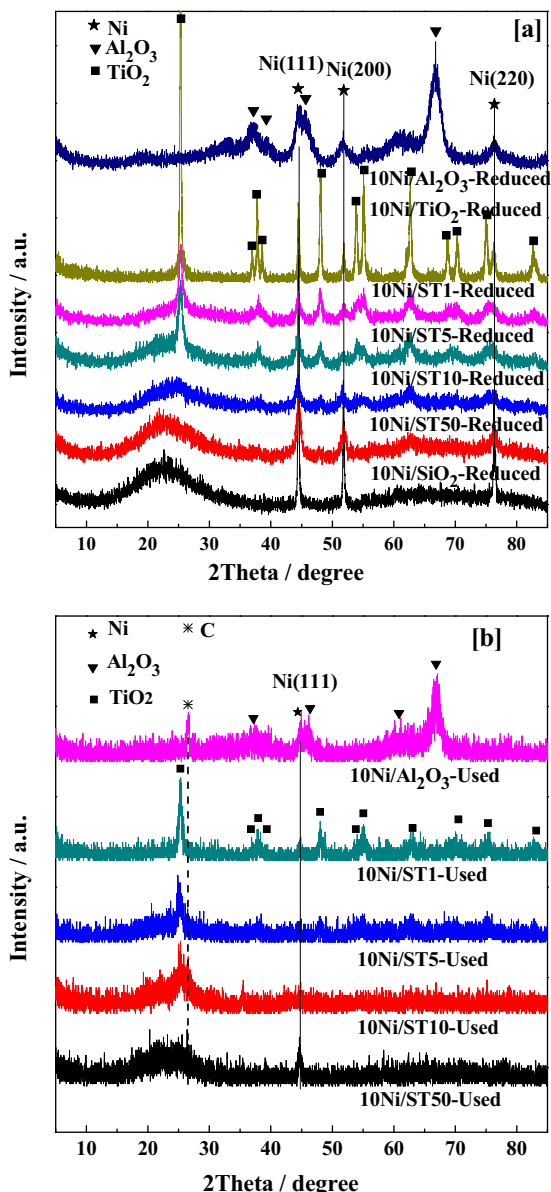
3.1.1. XRD

Fig. 1 shows the XRD patterns of the catalysts. As shown in Fig. 1a, it can be observed that all of the reduced catalysts displayed metallic Ni diffraction peaks at 2θ ($2\theta = 44.370^\circ, 51.890^\circ$, and 76.410° , JCPDS no. 65–2865), which can be ascribed to the (111), (200), and (220) plane of metallic Ni, respectively [18]. Among these reduced catalysts, 10Ni/ST5 displayed the weakest intensity of peaks for the metallic Ni phase, suggesting 10Ni/ST5 owns the highest dispersion of Ni therein (see Table 1). For the reduced catalysts 10Ni/ST5, 10Ni/ST1, and 10Ni/TiO₂, some XRD peaks corresponding to anatase TiO₂ crystals could be found and increased slightly with decreasing Si/Ti atomic ratio, which indicates the formation of crystalline TiO₂. However, the 10Ni/ST10 and 10Ni/ST50 reduced catalysts showed no diffraction peaks corresponding to Ti species, implying that the Ti⁴⁺ ions entered the SiO₂ network and took the place of some Si⁴⁺ ions, and thus leading to a homogeneous distribution of Ti⁴⁺ species in the silica matrix, the evidence for the presence of Ti(IV) with four ligands was reported in our previous publication [24]. Our previous results implied that when the Si/Ti mole ratio was about 10, the content of Ti(IV) in the SiO₂/TiO₂ composite supports may have reached a threshold for the existence of Si–O–Ti bonds. At Si/Ti < 10, a phase corresponding to the separa-

Table 1

Physical and chemical properties of catalysts.

Catalyst	S_{BET} ($\text{m}^2 \text{ g}^{-1}$) ^a	V_p ($\text{cm}^3 \text{ g}^{-1}$) ^b	Pore size (nm) ^c	Ni average crystallite size (nm) ^d	D_{Ni} (%) ^e	TOF_{CO} , 210 °C ($\times 10^{-3} \text{ S}^{-1}$) ^f	Ni content (wt%) ^g
10Ni/ST50-Reduced	542.5	0.63	3.38	12.9	24.3	1.79	9.91
10Ni/ST10-Reduced	469.7	0.61	3.90	13.5	23.9	1.60	10.11
10Ni/ST5-Reduced	346.7	0.50	8.18	9.7	35.6	3.06	9.91
10Ni/ST1-Reduced	290.0	0.39	4.17	15.7	22.7	2.73	10.19
10Ni/ γ -Al ₂ O ₃ -Reduced	148.9	0.43	8.55	22.1	20.1	0.98	9.94
10Ni/TiO ₂ -Reduced	–	–	–	25.5	10.9	1.43	
10Ni/SiO ₂ -Reduced	–	–	–	21.1	13.4	1.32	
10Ni/ST50-Used	352.8	0.54	4.34	–	–	–	9.51
10Ni/ST10-Used	246.0	0.37	4.37	–	–	–	9.73
10Ni/ST5-Used	248.2	0.46	5.21	–	–	–	9.72
10Ni/ST1-Used	152.0	0.31	6.08	–	–	–	9.87
10Ni/ γ -Al ₂ O ₃ -Used	102.0	0.32	8.23	–	–	–	9.30

^a Surface area obtained by using BET method.^b Pore volume obtained based on the nitrogen adsorbed volume at the relative pressure of 0.997.^c The average pore size of the catalysts based on the BJH adsorption.^d Calculated based on the Scherrer equation from XRD peak of Ni (111).^e Ni dispersion of the catalysts calculated according to the H₂ pulse adsorption.^f Calculated according to Ni dispersion and CO conversion of the catalysts at 210 °C.^g Ni content (wt%) of the catalysts measured by using inductively coupled plasma (ICP) analysis.**Fig. 1.** XRD patterns of the reduced catalysts (a) and used catalysts (b).

tion of anatase TiO₂ crystals appeared in the ST composite. For the reduced 10Ni/ γ -Al₂O₃ catalyst, diffraction peaks corresponding to γ -Al₂O₃ (JCPDS no. 10-0425) could be observed.

Fig. 1b shows the XRD patterns of the used catalysts. As can be seen, the 10Ni/ST10 used catalyst showed some peaks corresponding to anatase TiO₂ crystals, suggesting TiO₂ phase separation in the ST composite support after the long-term (144 h) stability test at 600 °C. This can be attributed to cleavage of the Si—O—Ti bond in the composite at high temperature. In addition, it can be observed that the peaks at 2 θ value of 26.603° (JCPDS no. 26-1079), which belongs to the diffraction peak of graphite. Among these catalysts, 10Ni/ γ -Al₂O₃ and 10Ni/ST10 catalysts have stronger intensities of peaks for graphite than others, revealing that the both catalysts are more likely to undergo coking, and thus the catalysts have much more graphite carbon species, which corresponds to the results of O₂-TPO and Raman spectroscopic analysis (see Section 3.1.7 and 3.1.8). Except for the 10Ni/ST5 used catalyst, the intensities of the Ni peaks for the other catalysts decreased. This may be attributed to sintering of the active Ni and its encapsulation in deposited carbon species, thereby decreasing its uniform dispersion, then resulting in the decreasing of signal in XRD patterns.

3.1.2. N_2 adsorption

N_2 adsorption–desorption isotherms and pore size distribution curves of the catalysts are shown in Fig. 2, and details of their physical properties are listed in Table 1. As presented in Fig. 2a, all of the reduced catalysts displayed type IV N_2 adsorption–desorption isotherms, and showed H₂ hysteresis loops (according to IUPAC classification), which indicates the presence of mesoporous structure in the reduced catalysts. From Table 1, it can be seen that the 10Ni/ST50 reduced catalyst had the highest specific surface area ($542.5 \text{ m}^2 \text{ g}^{-1}$) and pore volume ($0.63 \text{ cm}^3 \text{ g}^{-1}$) among the catalysts, the specific surface areas and pore volumes of the other catalysts decreasing slightly with increasing Ti content. The pore size distribution curves show that the 10Ni/ γ -Al₂O₃ reduced catalyst had a wide pore size distribution with an average value of about 8.55 nm; the 10Ni/STx ($x = 50, 10, 5, 1$) reduced catalysts showed narrow pore size distributions.

Fig. 2b displays the N_2 adsorption–desorption isotherms and pore size distribution curves of the used catalysts. All of the used catalysts still showed type IV N_2 adsorption–desorption isotherms, with H₂ hysteresis loops at high relative pressure, suggesting that they retained the mesoporous structure after long-term (144 h) stability tests at 600 °C. It can be observed that the specific sur-

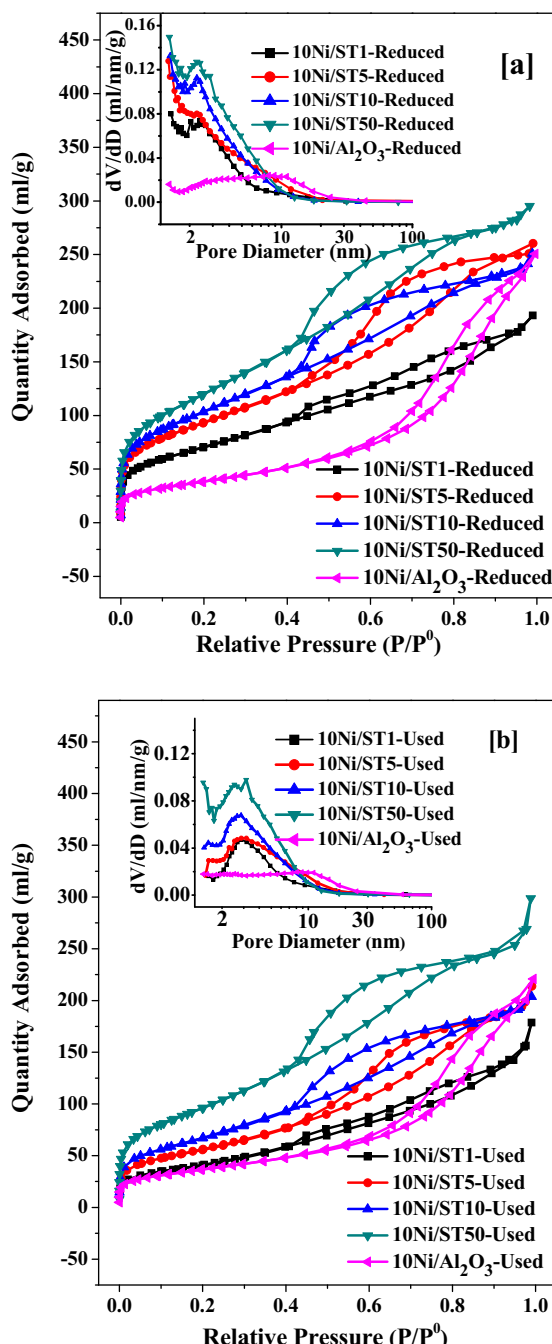


Fig. 2. The N₂ adsorption-desorption isotherms and distributions of pore size of the reduced catalysts (a) and used catalysts (b).

face areas and pore volumes of the used catalysts were lower than those of the corresponding reduced catalysts, which can be attributed to sintering and carbon deposition. Among the used catalysts, 10Ni/ST10 showed the most marked decreases in specific surface area and pore volume, amounting to 47.6% and 39.3%, respectively (see Table 1), ultimately leading to catalyst deactivation. The micropore structure in 10Ni/ST_x ($x=50, 10, 5, 1$) was modified, so that the pore size became larger.

3.1.3. TEM

TEM and particle statistical distribution images of the 10Ni/ST5, 10Ni/ST10, and 10Ni/γ-Al₂O₃ reduced catalysts are presented Fig. 3. It can be seen that active Ni particles were uniformly dispersed in these catalysts. Compared to the 10Ni/ST10 and 10Ni/γ-Al₂O₃

Table 2
The Proportion of the different reduction peaks areas for catalysts.

Catalysts	The Proportion of the different reduction peaks areas through H ₂ -TPR (%)		
10Ni/γ-Al ₂ O ₃	34.2 (477 °C) ^a	50.7 (558 °C)	15.1 (730 °C)
10Ni/TiO ₂	61.9 (353 °C)	21.9 (420 °C)	16.2 (621 °C)
10Ni/ST1	16.3 (371 °C)	24.3 (429 °C)	59.4 (520 °C)
10Ni/ST5	13.1 (355 °C)	20.6 (416 °C)	66.3 (496 °C)
10Ni/ST10	14.3 (362 °C)	25.0 (418 °C)	60.7 (475 °C)
10Ni/ST50	38.1 (357 °C)	40.0 (426 °C)	21.9 (498 °C)
10Ni/SiO ₂	75.3 (368 °C)	24.7 (454 °C)	–

^a the T_{max} of the reduction peak.

reduced catalysts, 10Ni/ST5 showed higher Ni dispersion and smaller Ni particle size. There are two possible reasons for this: (1) ST5 may provide the appropriate metal–support interaction and thereby promote the dispersion of Ni, such that the catalyst possesses more suitable active Ni species for CO methanation; (2) a TiO₂ phase corresponding to anatase micro-separation appeared in the ST5 composite support, and an appropriate amount of TiO₂ may serve as an electronic promoter [22], effectively facilitating dispersion of the Ni catalyst. According to the particle size statistical analysis, the average Ni particle sizes of 10Ni/γ-Al₂O₃, 10Ni/ST10, and 10Ni/ST5 were 13.85, 13.21, and 8.81 nm, respectively, as determined from the statistics of more than 200 randomly measured particles, which would have acceptable accuracy. Thus, the 10Ni/ST5 reduced catalyst had the smallest Ni particle size, and hence the greatest dispersion and active specific surface area of Ni, which effectively improved its catalytic activity and CH₄ selectivity in CO methanation. This result was consistent with that of the XRD characterization.

3.1.4. H₂-TPR

The metal–support interaction was conducted using H₂-TPR measurements. The H₂-TPR profiles of the 10Ni/SiO₂, 10Ni/TiO₂, 10Ni/γ-Al₂O₃, and 10Ni/ST_x ($x=50, 10, 5, 1$) catalysts are shown in Fig. 4. For these catalysts, based on the positions of the reduction peaks from NiO species, these peaks can be classified into three stages (α -, β -, and γ -stages). The reduction peaks of α -stage in the low-temperature region (280–390 °C) can be attributed to the reduction of NiO species, which interacts weakly with the support and exists in the nature in free form. The reduction peak of NiO species with moderately interacting with the support belongs to the β -stage (390–670 °C). Generally, the active species of β -stage can contribute to CO methanation. The γ -stage in the high-temperature region (670–870 °C) belongs to the reduction of NiO species, which interacts strongly with support, and it is difficult to reduce [25]. As shown in Fig. 4, no reduction peak corresponding to the α -stage was found for 10Ni/γ-Al₂O₃, indicating a strong interaction between NiO species and γ-Al₂O₃. Compared to the 10Ni/SiO₂ catalyst, it can be seen that the temperatures of reduction peaks of the catalysts 10Ni/ST_x ($x=50, 10, 5, 1$) slightly shifted to higher temperatures with increasing titanium content in the mixed SiO₂/TiO₂ oxides, suggesting that this can improve the interaction between NiO and the ST composite support. Table 2 lists quantitative H₂-TPR results for the catalysts according to Gaussian distributions. Among the catalysts, it can be seen that 10Ni/ST5 had the highest fraction of β -stage (86.9%), which facilitates CO methanation. From the observed catalytic activity (see Section 3.2.1), 10Ni/ST5 showed the best catalytic performance. The results reveal that the ST5 support can provide suitable metal–support interaction. The 10Ni/ST5 catalyst possesses many more suitable Ni active species, which is beneficial for CO methanation, demonstrating a good support effect of ST5 and a good synergistic effect at the interface between the metal and support.

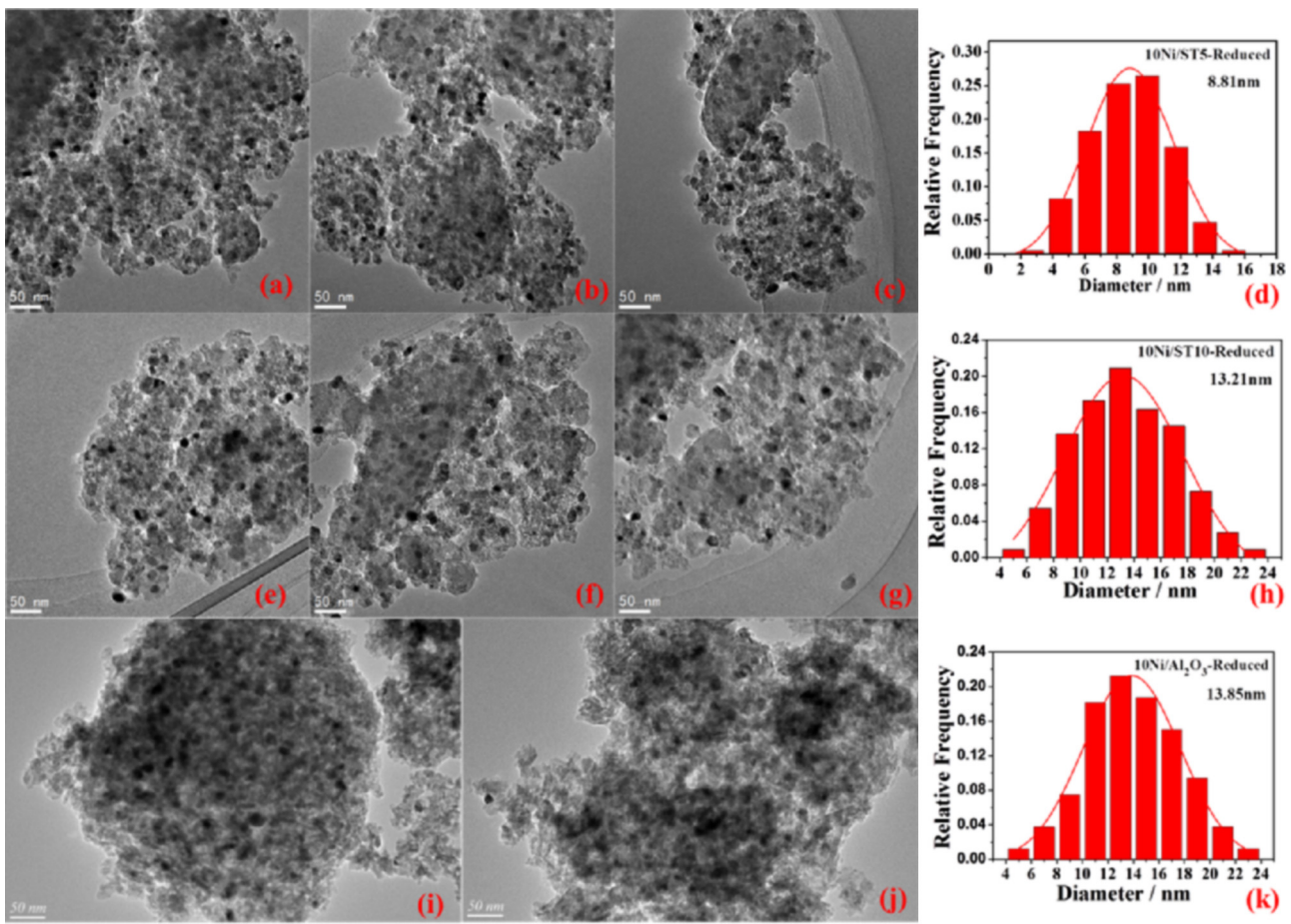


Fig. 3. TEM and particle statistical distribution images of the 10Ni/ST5 (a–d), 10Ni/ST10, (e–h), 10Ni/γ-Al₂O₃ (i–k) reduced catalysts.

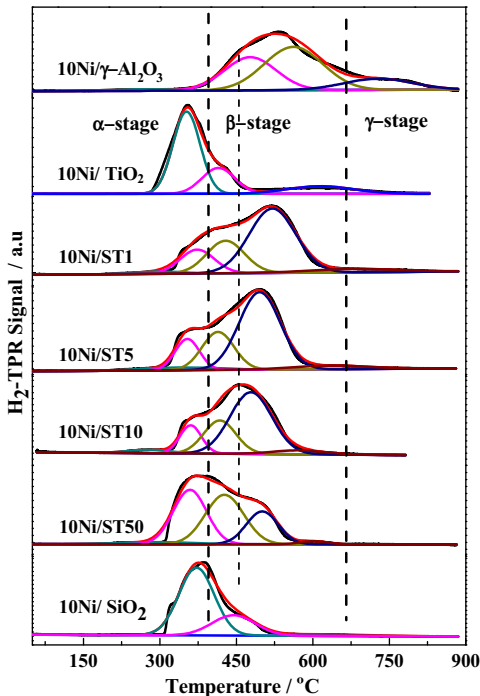


Fig. 4. H₂-TPR profiles of the catalysts.

3.1.5. H₂-TPD

Fig. 5 shows H₂-TPD profiles for each of the samples. As shown in Fig. 5, for the reduced catalysts, the peaks in the range of the low temperature (<450 °C) correspond to desorption of hydrogen weakly chemisorbed on the surface of active Ni. The high-temperature desorption peaks (>450 °C) belong to hydrogen strongly chemisorbed on the surface and sub-surface of catalyst. They may also be related to H₂ chemisorbed on the Ni sub-surface or spillover H₂, which would improve H₂ storage capacity [18]. The 10Ni/ST5 reduced catalyst displayed the most intense H₂ desorption peak in the H₂-TPD profiles, suggesting that it had greater Ni dispersion and more abundant dissociated active H. This may be ascribed to the anatase TiO₂ crystals separated from the ST composite support, an appropriate amount of which serves as an electronic promoter and improves the dispersion of Ni. The 10Ni/ST5 reduced catalyst showed the strongest H₂ adsorption capacity and highest Ni dispersion (35.6%, see Table 1). The interaction between Ni and the adsorbed H₂ could be investigated on the basis of H₂ desorption peak positions. The temperature of the H₂ desorption peak for 10Ni/γ-Al₂O₃ was the highest, revealing that this catalyst had the strongest interaction between active Ni and adsorbed H₂. In addition, it can be observed that *T*_{max} of the H₂ desorption peaks for 10Ni/ST_x (_x = 50, 10, 5, 1) slightly shifted to higher temperature with increasing Ti content in the ST composite support, suggesting that this enhanced the interaction between active Ni and adsorbed H₂. The conclusion is similar to that from the H₂-TPR data: the metal–support interaction gradually increases with increasing Ti content in the ST composite support.

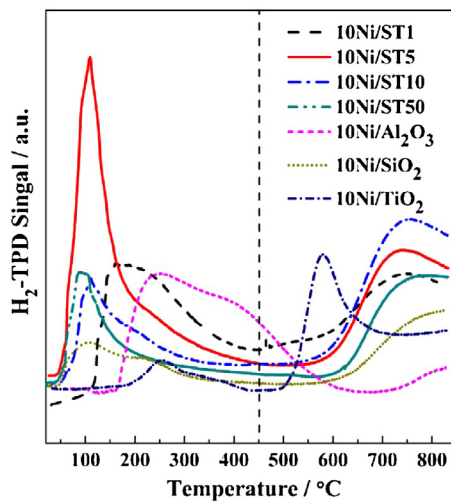


Fig. 5. H_2 -TPD profiles of the catalysts.

3.1.6. XAFS

The Ni K-edge XANES and EXAFS spectra for Ni foil, NiO , and the Ni-based catalysts are presented in Fig. 6, which provides information about the different oxidation states for the Ni species (Ni or NiO_x). The catalysts were reduced with H_2 in situ in the instrument before XAFS measurement. As shown in Fig. 6a, the Ni foil and NiO reference sample gave different XANES spectra. The Ni foil showed several typical absorption peaks at 8333, 8348, and 8358 eV, whereas a peak at 8349 eV was observed for NiO [26–28]. It can be observed that the XANES spectra about the 10Ni/SiO₂, 10Ni/TiO₂, and 10Ni/ST50 catalysts were similar to that of Ni foil, which indicates that the NiO in these catalysts with H_2 was almost reduced to Ni. The results also imply a weak interaction between the metal and support compared to those in the other catalysts. The Ni K-edge XANES spectra of the 10Ni/ST10, 10Ni/ST5, and 10Ni/ST1 catalysts closely resemble that of Ni, indicating that Ni species in these catalysts were largely reduced to Ni metal. Nevertheless, reduction of NiO species in the 10Ni/ST10, 10Ni/ST5, and 10Ni/ST1 catalysts is less facile than in the 10Ni/SiO₂, 10Ni/TiO₂, and 10Ni/ST50 catalysts, suggesting that these catalysts have stronger metal–support interactions. This is in accordance with the results of H_2 -TPR analysis.

Fourier transforms (radial structure function, RSF) of Ni *K*-edge k^3 -weighted EXAFS spectra for Ni-based catalysts are presented Fig. 6b. All of the reduced catalysts showed peaks corresponding to Ni–O bonds at 0.9–1.9 Å [26,27], indicating the existence of NiO species. The absorption peaks belong to the Ni–Ni bonds for Ni metal at the range of 1.8–2.5 Å, the intensity of which decreased in the order: 10Ni/TiO₂ > 10Ni/ST1 > 10Ni/SiO₂ > 10Ni/ST50 > 10Ni/ST10 > 10Ni/ST5. Generally speaking, the intensities of these peaks gradually increase with increasing average crystallite size of corresponding metal species in the RSF [26]. The peak strength for the Ni–Ni bond represents the coordination number thereof, and the larger the coordination number, the larger the Ni crystallite size. The 10Ni/TiO₂ catalyst had the largest Ni crystallite size, while the 10Ni/ST5 catalyst had the smallest, as nearly borne out by the XRD results. Furthermore, there were small Ni crystals in the 10Ni/ST5 catalyst, suggesting high Ni dispersion and more active Ni sites, thus enhancing its catalytic performance in CO methanation (see Section 3.2.1).

3.1.7. SAED and O_2 -TPO analysis

Fig. 7 shows the morphological characteristics of the catalysts after long-term (144 h) stability tests. As indicated in Fig. 7, the used catalyst underwent Ni sintering and coking. Among the

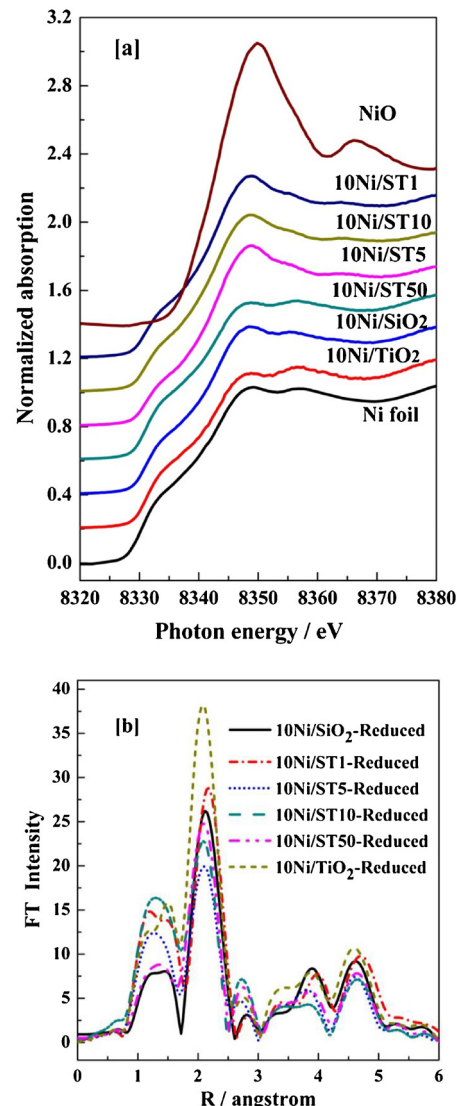


Fig. 6. The Ni K-edge XANES spectra of Ni foil, NiO and Ni-based catalysts (a) and Fourier transform spectra of Ni K-edge k^3 -weighted EXAFS for Ni-based catalysts (b).

used catalysts, 10Ni/ST5 retained good Ni dispersion and small Ni particle size, and only a small amount of carbon whisker was observed thereon. This can be attributed to separation of an appropriate amount of TiO_2 , which serves as an electronic promoter and improves Ni dispersion. In the 10Ni/ST10 and 10Ni/γ-Al₂O₃ used catalysts, the active Ni particles underwent significant sintering, increasing to a size of about 100 nm. It can be seen that some of the Ni in the catalyst was encapsulated by carbon fibers. The diameter of the carbon fibers was similar to that of the Ni particles, and carbon fibers gradually grew along the Ni particles. Previous results have shown that the formation of the carbon fiber is related to the size of the Ni particles [29–31]. On this basis, we surmise that the larger the Ni particles, the larger and more extensive the carbon fibers produced [32,33]. Therefore, it should be possible to inhibit coking of the catalyst by controlling the size of the active Ni particles [34,35]. In addition, selected-area electron diffraction (SAED; Fig. 7(e, f, h, i)) patterns of the 10Ni/ST10 and 10Ni/γ-Al₂O₃ used catalysts were measured. The SAED patterns in Fig. 7(e, i) are concentric and ring-shaped, indicating a microstructure consisting of two different areas with alternating contrast, suggesting that some carbon fiber was graphitized and acquired a microcrystalline

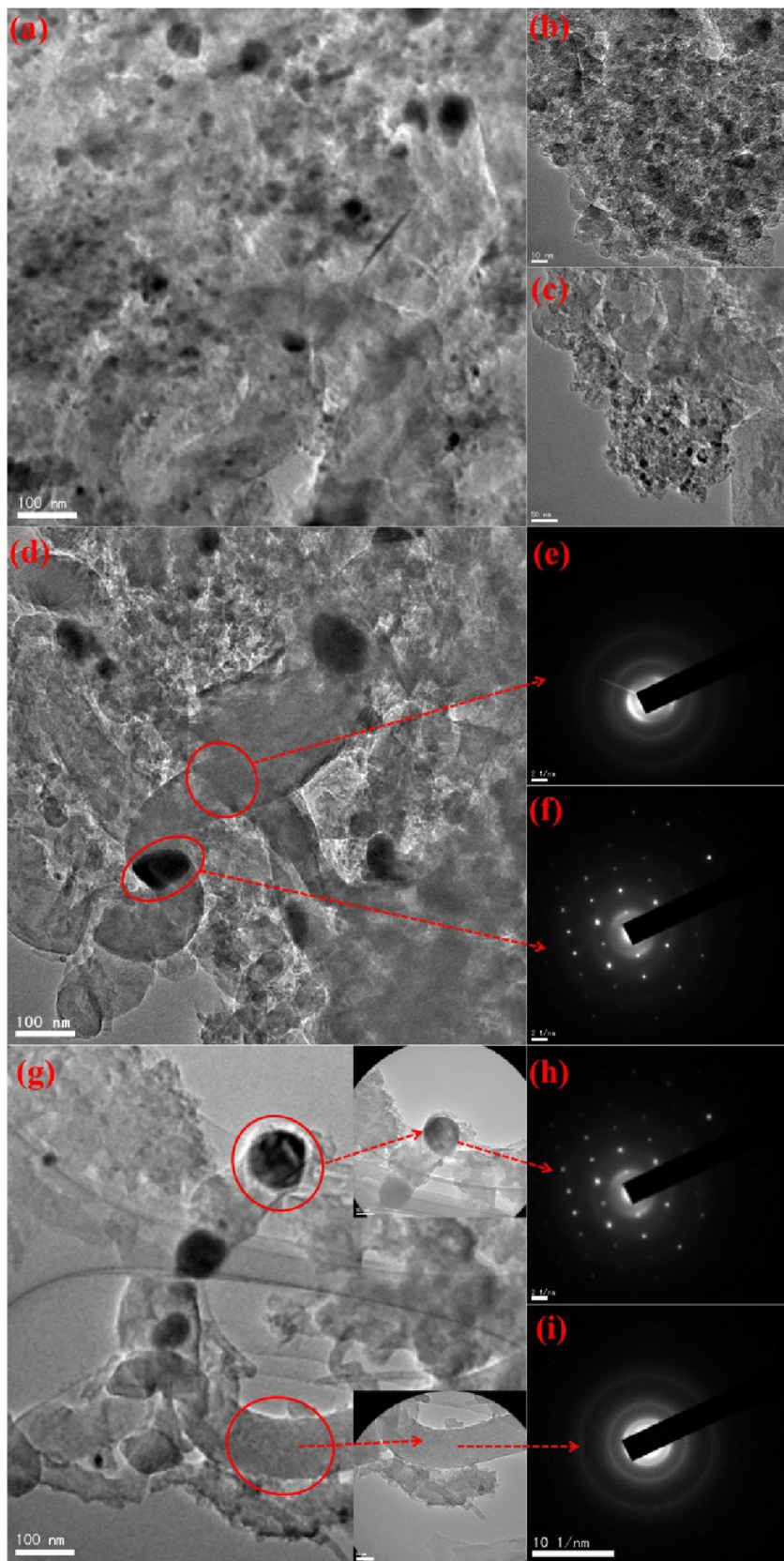


Fig. 7. TEM images of the 10Ni/ST5 (a–c), 10Ni/ST10 (d–f), 10Ni/γ-Al₂O₃ (g–i) used catalyst samples.

structure with long-range order [36]. In addition, the contrast in the concentric ring-shaped SAED pattern of the 10Ni/γ-Al₂O₃ used catalyst was more marked than that in the pattern of the 10Ni/ST10

catalyst, suggesting a higher degree of graphitization of the carbon fiber in the former. This is consistent with the results of Raman spectroscopic and O₂-TPO analyses. Highly symmetrical spots were

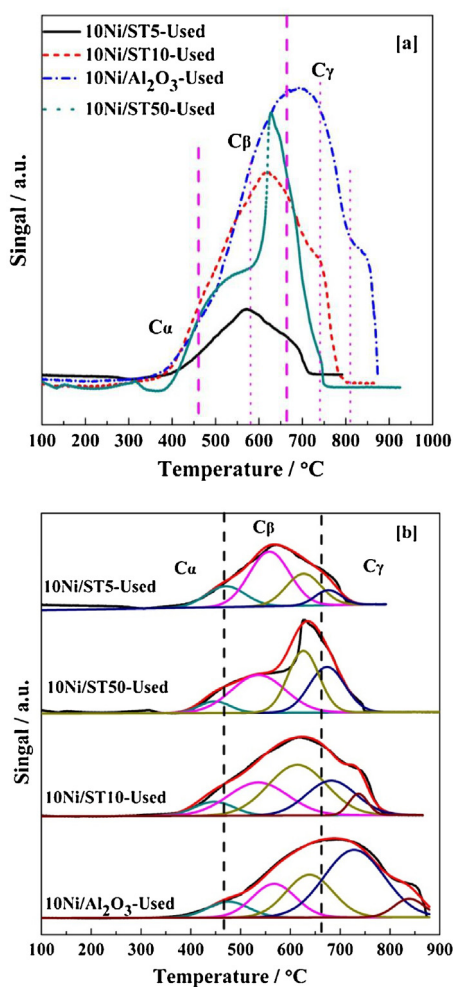


Fig. 8. O_2 -TPO profiles of the used catalyst samples.

seen in the SAED patterns (Fig. 7(f, h)), showing that the Ni particles were in a single-crystal state. At the same time, concentric rings were seen in the diffraction patterns, indicating that the Ni particles were encapsulated by carbon fibers.

Fig. 8 shows the O_2 -TPO profiles of the used catalysts. Based on the positions for CO_2 peak, and the previous literature data [12,31,37–40], the deposited carbon species can be mainly divided into three types: amorphous surface active carbon species ($\text{C}\alpha$, $<460^\circ\text{C}$); carbon whiskers, filaments, and fibers ($\text{C}\beta$, $460\text{--}660^\circ\text{C}$); graphite carbon and some carbon fibers with graphitization ($\text{C}\gamma$, $>660^\circ\text{C}$). Regarding the activities of these deposited carbon species reacting with oxygen, it demonstrates the following decreasing tendency: $\text{C}\alpha > \text{C}\beta > \text{C}\gamma$. $\text{C}\alpha$ as the main active species plays the key role for the formation of CH_4 in CO methanation, whereas the accumulation of $\text{C}\gamma$, the most inactive species, takes the responsibility for the deactivation of the catalyst. From Fig. 8b, it is evident that at least three types of the deposited carbon species existed on the catalyst. As shown in Fig. 8, among the catalysts, the O_2 -TPO peak intensity for $10\text{Ni}/\gamma\text{-Al}_2\text{O}_3$ was the strongest, which suggests that it contained the largest amount of coke. This may have been because the $\gamma\text{-Al}_2\text{O}_3$ support had more acidic B sites [38]. At the same time, the experimental results of stability evaluation showed the $10\text{Ni}/\gamma\text{-Al}_2\text{O}_3$ catalyst to be the least stable, having the greatest amount of deposited carbon (especially graphite carbon and carbon fibers with graphitization), implying that increasing amount of deposited carbon can gradually lead to catalyst deactivation. The tendency for carbon deposition on the catalysts decreased in

Table 3
Results of O_2 -TPO and Raman spectroscopy analyses for used catalyst samples.

Catalysts	Proportion of different carbon species through O_2 -TPO (%)			Peak intensities ratio through Raman spectroscopy (%)	
	$\text{C}\alpha$	$\text{C}\beta$	$\text{C}\gamma$	I_G/I_{Total}	I_G/I_{D1}
10Ni/ST5-Used	17.9	73.3	8.8	9.9	20.6
10Ni/ $\gamma\text{-Al}_2\text{O}_3$ -Used	7.5	39.8	52.7	21.9	47.1
10Ni/ST50-Used	7.2	64.8	28.0	18.8	42.8
10Ni/ST10-Used	6.1	61.5	32.4	14.5	29.9

the order: $10\text{Ni}/\gamma\text{-Al}_2\text{O}_3 > 10\text{Ni}/\text{ST10} > 10\text{Ni}/\text{ST50} > 10\text{Ni}/\text{ST5}$. From Fig. 8(b) and Table 3, it is evident that $10\text{Ni}/\gamma\text{-Al}_2\text{O}_3$ had a greater relative amount of $\text{C}\gamma$ carbon species than the other catalysts, which implies that the $\gamma\text{-Al}_2\text{O}_3$ support is more inclined to produce graphitic carbon. This is because the $10\text{Ni}/\gamma\text{-Al}_2\text{O}_3$ catalyst has more active sites for dehydrogenation, making it easy to generate catalytic carbon (typically carbon fibers and graphitic carbon). The deposited carbon species on the $10\text{Ni}/\text{ST5}$, $10\text{Ni}/\text{ST10}$, and $10\text{Ni}/\text{ST50}$ used catalysts were mainly fibers and filaments. The $10\text{Ni}/\text{ST5}$ used catalyst had the highest relative amount of $\text{C}\alpha$ carbon species and the lowest relative amount of $\text{C}\gamma$ carbon species. Combined with the results of TEM analysis, it could be inferred that the deposited carbon species on the $10\text{Ni}/\text{ST5}$ catalyst were mainly amorphous carbon and carbon whiskers, and that the total amount of deposited carbon was small. The $10\text{Ni}/\text{ST5}$ catalyst showed good stability and was not susceptible to deactivation. The results may be related to the appropriate amount of separated TiO_2 from ST5 playing the role of an electronic promoter, changing the form of the active Ni and the chemical reaction micro-environment of the raw gas in the process.

3.1.8. Raman spectroscopic analysis

The chemical structures of carbon species such as graphite crystallites can be identified by Raman measurements. Generally, carbon species with an ordered structure give rise to two main absorption bands in Raman spectra; that at $\nu = 1580\text{ cm}^{-1}$ can be attributed to the vibration absorption peak of the graphite structure, E_{2g}^2 , and that at $\nu = 1350\text{ cm}^{-1}$ can be attributed to the absorption peak of carbon species with a disordered structure. However, for the Raman spectra of carbon species with disordered structure, there is greater overlap of the absorption peaks, and the overlapping areas hide structural information, such as some graphite or graphite-like structure. Therefore, more information about the structure of carbon species may be gleaned by applying a peak-fitting method. Fig. 9 shows the Raman spectra of the used catalysts. Based on previous literature reports [41,42], we carried out peak fitting of these Raman spectra to extract more information about the structures of the carbon species. The bands at $\nu = 1150, 1350, 1500, 1580$, and 1620 cm^{-1} for five Gaussian fitted peaks are designated as the D_4 -, D_1 -, D_3 -, G -, and D_2 -bands, respectively. In addition, the higher the I_G/I_{D1} ratio, the greater the degree of graphitization of the carbon species. As indicated in Fig. 9 and Table 3, among the used catalysts, $10\text{Ni}/\gamma\text{-Al}_2\text{O}_3$ had the highest I_G/I_{total} (21.9%) and I_G/I_{D1} (47.1%) ratios for deposited carbon, whereas $10\text{Ni}/\text{ST5}$ had the lowest I_G/I_{total} (9.9%) and I_G/I_{D1} (20.6%) ratios, suggesting that the former contained much more graphitic and graphite-like carbon species [41,43] than the latter.

3.2. CO methanation

3.2.1. Catalytic activities

Fig. 10 displays the catalytic performances of the catalysts in CO methanation under conditions of 1.0 MPa , a WHSV of $15000\text{ mL g}^{-1}\text{ h}^{-1}$, and $190\text{--}450^\circ\text{C}$. From Fig. 10a, it is evident that

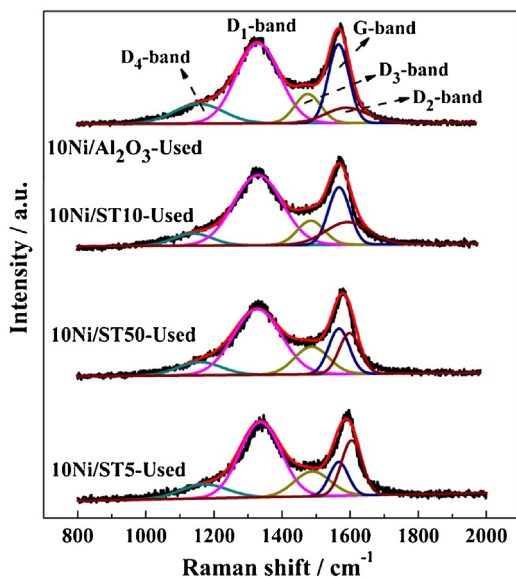


Fig. 9. Curve fitting of Raman spectra of the used catalysts.

the CO conversion for these catalysts increased with increasing reaction temperature up to 270 °C, and that it kept stable in the relatively high temperatures (350–450 °C). Among the catalysts, 10Ni/SiO₂ showed the lowest CO conversion below 330 °C. The CH₄ selectivities of these catalysts increased significantly with increasing reaction temperature up to 350 °C, and the 10Ni/ST5 catalyst showed the best CH₄ selectivity (95.6%, 370 °C; Fig. 10b). As shown in Fig. 10c, compared with both the 10Ni/SiO₂ and 10Ni/TiO₂ catalysts, the 10Ni/STx catalysts gave higher CH₄ yields, implying that the ST composite oxides imparted a better support effect. The 10Ni/ST5 catalyst gave the best CH₄ yield. The CH₄ yields decreased in the order 10Ni/ST5 > 10Ni/ST1 > 10Ni/ST50 > 10Ni/ST10 > 10Ni/γ-Al₂O₃ > 10Ni/TiO₂ > 10Ni/SiO₂ for high CO concentration methanation at 290 °C, further indicating that the SiO₂/TiO₂ composite supports can provide suitable metal–support interactions, facilitating the formation of β-stage Ni.

Among the 10Ni/STx catalysts, 10Ni/ST10 gave the lowest CH₄ yield. This can be attributed to the fact that it had the most B sites [24], which promote the dehydrogenation of CH₄. The 10Ni/ST5 and 10Ni/ST1 catalysts gave higher CH₄ yields than 10Ni/ST50 and 10Ni/ST10. This can be attributed to the separation of TiO₂ from the Si–O–Ti bonds of mixed STx ($x = 5, 1$), which can trigger electron

transfer and significantly increases the electron cloud density of nickel species ($\text{Ni}^0 \rightarrow \text{Ni}^{\delta-}$) (See Supplementary information), thereby weakening the C–O bond of the Ni–C–O moiety and facilitating the dissociation of CO. The fact that the highest CH₄ yield was seen with 10Ni/ST5 can be attributed to both the optimal metal–support interaction and consequent highest Ni dispersion and most β-stage Ni species, as well as the optimal amount of separated TiO₂ as an electron promoter, which facilitates CO dissociation. Calculated TOF values about CO conversion for these catalysts in CO methanation at low CO conversion under the conditions of 210 °C, and a high WHSV (15,000 mL g⁻¹ h⁻¹) are listed in Table 1. TOF values for the catalysts decrease in the order 10Ni/ST5 (3.06×10^{-3} s⁻¹) > 10Ni/ST1 (2.73×10^{-3} s⁻¹) > 10Ni/ST50 (1.79×10^{-3} s⁻¹) > 10Ni/ST10 (1.60×10^{-3} s⁻¹) > 10Ni/TiO₂ (1.43×10^{-3} s⁻¹) > 10Ni/SiO₂ (1.32×10^{-3} s⁻¹) > 10Ni/γ-Al₂O₃ (0.98×10^{-3} s⁻¹). The results confirm that the catalysts consisting of Ni supported on composite oxides have higher catalytic activity than those in which Ni is supported on a single oxide, suggesting that the composite supports have a better synergistic effect with the metal.

3.2.2. Catalyst stability

Fig. 11 shows the results of stability tests on the catalysts at 500 and 600 °C under 1.0 MPa with a WHSV of 30,000 mL g⁻¹ h⁻¹. As shown in Fig. 11, CO conversions, CH₄ selectivities, and CH₄ yields with the 10Ni/ST10, 10Ni/ST50, and 10Ni/γ-Al₂O₃ catalysts were significantly reduced. Moreover, the decreases in these parameters in two time periods (40–80 h, 120–144 h) at 600 °C were distinctly higher than those for the catalysts deployed at 500 °C in two time periods (0–40 h, 80–120 h). The results are due to the fact that the catalysts are more likely to undergo Ni sintering and CH₄ cracking reaction at 600 °C, which can lead to carbon deposition. In particular, among the 10Ni/STx ($x = 50, 10, 5, 1$) series of catalysts, CO conversion, CH₄ selectivity, and CH₄ yield with the 10Ni/ST10 catalyst decreased significantly relative to those with the other catalysts. This may be related to the fact that ST10 has many more B acid sites [24,44], which facilitate the dehydrogenation of hydrocarbons [45]. The 10Ni/ST5 catalyst not only gave the highest CH₄ yield, but also maintained relatively steady CO conversion, CH₄ selectivity, and CH₄ yield over the long-term (144 h) tests, and the ICP data also showed that there was negligible Ni leaching happened during the reaction (See Table 1). Again, this can be attributed to the aforementioned inhibitory effect of TiO₂ separated from the ST5 composite support on Ni sintering, such that the catalyst maintained small Ni particle size and high Ni dispersion (Fig. 7). The results indicate that varying the content of Ti species in SiO₂/TiO₂ by

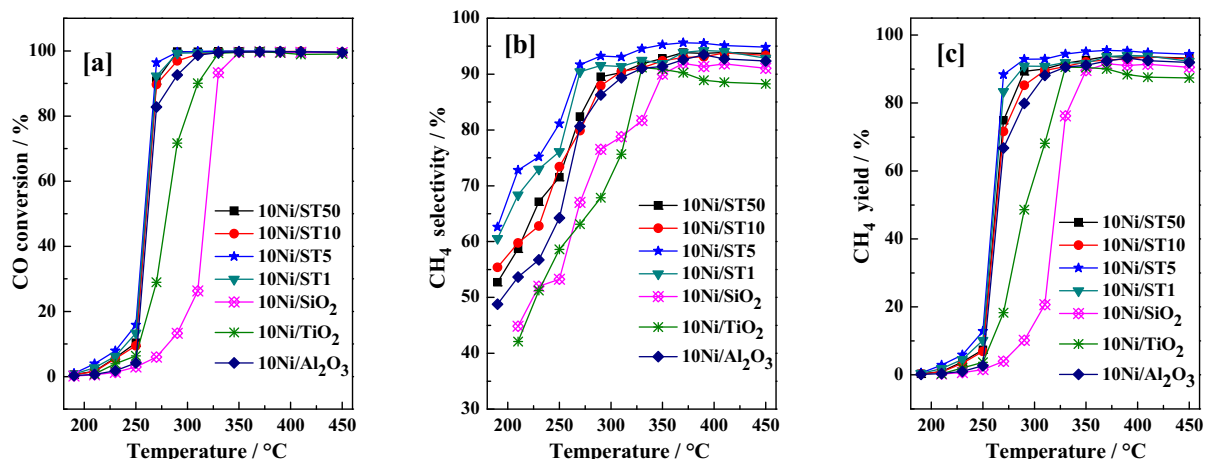


Fig. 10. CO conversion (a), CH₄ selectivity (b) and CH₄ yield (c) of the catalysts (Reaction conditions: WHSV = 15000 mL g⁻¹ h⁻¹, V(H₂)/V(CO) = 3, P = 1 MPa).

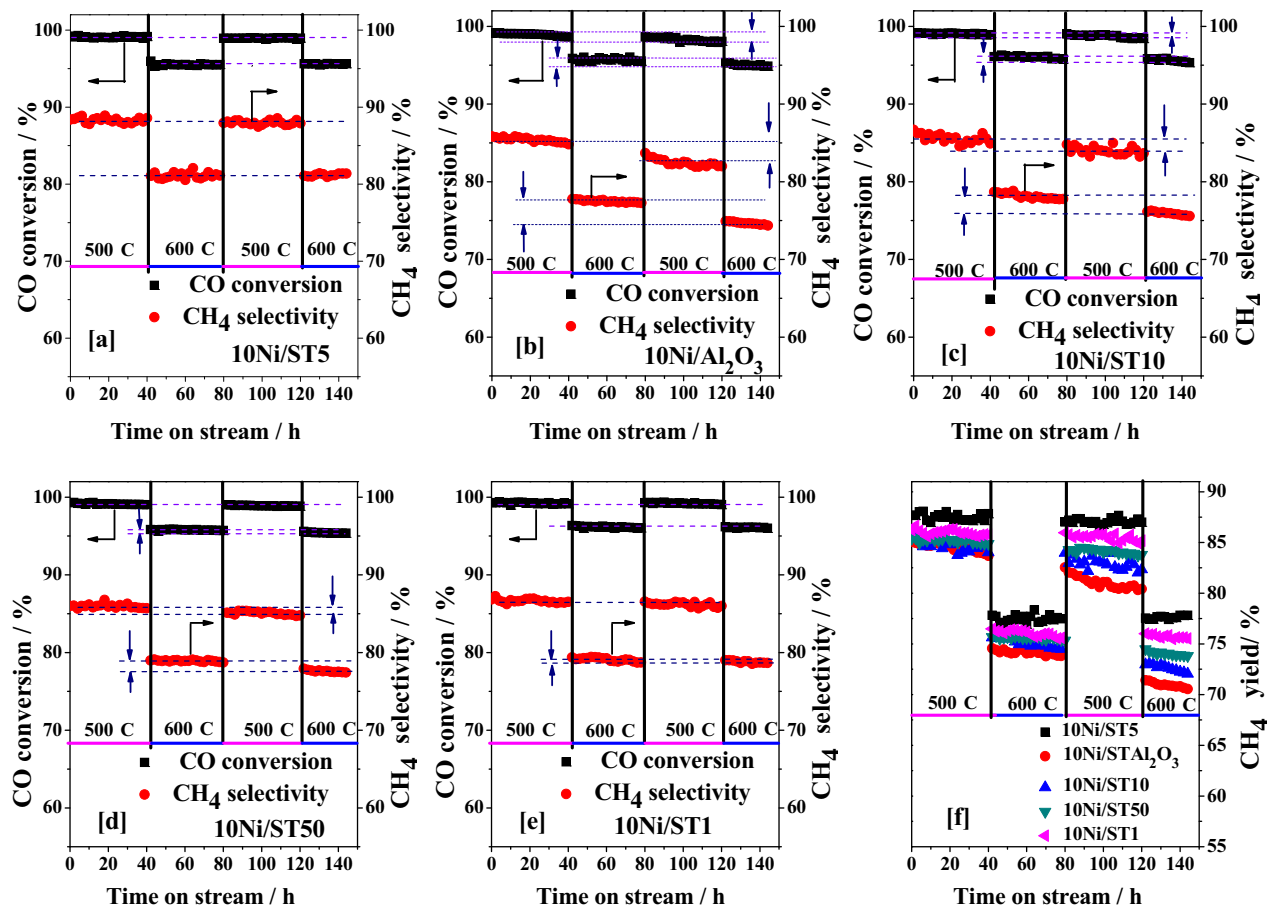


Fig. 11. long-term (144 h) stability results of the 10Ni/ST_x ($x=50, 10, 5, 1$) and 10Ni/γ-Al₂O₃ catalysts (Reaction conditions: WHSV = 30,000 mLg⁻¹ h⁻¹, V(H₂)/V(CO) = 3, P = 1 MPa).

adjusting the Si/Ti molar ratio significantly influences the catalytic performance. The CH₄ yields of these catalysts at 600 °C decrease in the order: 10Ni/ST5 > 10Ni/ST1 > 10Ni/ST50 > 10Ni/ST10 > 10Ni/γ-Al₂O₃, indicating that the 10Ni/ST_x ($x=50, 10, 5, 1$) catalysts have better high-temperature stability than 10Ni/γ-Al₂O₃. In summary, 10Ni/ST5 showed the best catalytic stability, whereas 10Ni/γ-Al₂O₃ showed the worst.

4. Conclusion

Composite oxides with different molar ratios of Si/Ti have been prepared by a template-free sol-gel method, and Ni/ST catalysts have been prepared through ultrasonic impregnation. The effects of Ti species on the catalytic activity, CH₄ selectivity, anti-sintering properties, and anti-coking properties of the catalysts have been investigated. The experimental results indicated that 10Ni/ST_x ($x=50, 10, 5, 1$) displayed higher catalytic performances than catalysts consisting of Ni supported on a single oxide, and the composite ST oxides showed good synergistic effects between the Ni and the support. Among these catalysts, 10Ni/ST5 showed the best catalytic activity (370 °C, CO conversion: 99.9%, CH₄ selectivity: 95.6%) as well as anti-sintering and anti-coking properties after long-term (144 h) stability tests. Moreover, experimental results have confirmed that the content of Ti in SiO₂/TiO₂ can influence the catalytic performances of the 10Ni/ST_x catalysts.

The composite ST supports have large specific surface area, large pore volume, and can provide suitable metal-support interactions. This can facilitate Ni dispersion, which endows these catalysts with more suitable Ni active sites for methanation. A TiO₂ phase cor-

responding to micro-separation of anatase appeared in the ST5 composite support, and an appropriate amount of TiO₂ can serve as an electronic promoter, not only effectively facilitating the dispersion of Ni and sintering of the catalyst, but also triggering electron transfer and enhancing the electron cloud density of Ni⁰⁰ (Ni⁰⁰ → Ni^{δ-}), which could weaken the C–O bond of the Ni–C–O moiety, facilitating the dissociation of CO, thereby improving the catalytic activity, selectivity, and anti-sintering and anti-coking properties of the catalyst.

In addition, experimental results of stability tests have revealed that the used catalysts contained at least three types of deposited carbon species: active carbon species, carbon fiber species (carbon whiskers, carbon filaments), and graphite carbon species. Compared to the other used catalysts, 10Ni/ST5 had the lowest amount of deposited carbon species and the best catalytic stability.

Acknowledgements

This work has been supported by a grant from the National Natural Science Foundation of China (21376159 and 21276169) and the National Scholarship Foundation of China. The authors would like to thank Prof. Yongfeng Hu from Canadian Light Source for his help with XAFS analysis.

Appendix A. Supplementary data

Supplementary data associated with this article can be found, in the online version, at <http://dx.doi.org/10.1016/j.apcatb.2016.08.061>.

References

- [1] X. Lin, K. Yang, R. Si, X. Chen, W. Dai, X. Fu, *Appl. Catal. B* 147 (2014) 585–591.
- [2] T. Li, S. Wang, D.N. Gao, S.D. Wang, *J. Fuel Chem. Technol.* 42 (2014) 1440–1446.
- [3] A. Boffa, C. Lin, A.T. Bell, G.A. Somorjai, *J. Catal.* 149 (1994) 149–158.
- [4] M.A.A. Aziz, A.A. Jalil, S. Triwahyono, S.M. Sidik, *Appl. Catal. A* 486 (2014) 115–122.
- [5] J. Li, L. Zhou, Q. Zhu, H. Li, *RSC Adv.* 5 (2015) 64486–64494.
- [6] M.A. Vannice, S.Y. Wang, S.H. Moon, *J. Catal.* 71 (1981) 152–166.
- [7] G.A. Mills, F.W. Steffgen, *Catal. Rev.* 8 (2006) 159–210.
- [8] Z. Qin, J. Ren, M. Miao, Z. Li, J. Lin, K. Xie, *Appl. Catal. B* 164 (2015) 18–30.
- [9] A. Kambolis, D. Ferri, Y. Lu, S.N. Yannopoulos, S. Pokrant, D. Rentsch, O. Kröcher, *ChemCatChem* 7 (2015) 3261–3265.
- [10] X. Dai, J. Liang, D. Ma, X. Zhang, H. Zhao, B. Zhao, Z. Guo, F. Kleitz, S. Qiao, *Appl. Catal. B* 165 (2015) 752–762.
- [11] P. Lakshmanan, M.S. Kim, E.D. Park, *Appl. Catal. A* 513 (2016) 98–105.
- [12] M.A. Lucchini, A. Testino, A. Kambolis, C. Proff, C. Ludwig, *Appl. Catal. B* 182 (2016) 94–101.
- [13] A.M. Abdel-Mageed, D. Widmann, S.E. Olesen, I. Chorkendorff, J. Biskupek, R.J. Behm, *ACS Catal.* 5 (2015) 6753–6763.
- [14] X. Lin, L. Lin, K. Huang, X. Chen, W. Dai, X. Fu, *Appl. Catal. B* 168 (2015) 416–422.
- [15] N. Shimoda, D. Shoji, K. Tani, M. Fujiwara, K. Urasaki, R. Kikuchi, S. Satokawa, *Appl. Catal. B* 174 (2015) 486–495.
- [16] B. Nematollahi, M. Rezaei, E.N. Lay, *Int. J. Hydrogen Energy* 40 (2015) 8539–8547.
- [17] Y. Huang, J. Wang, Z. Liu, G. Lin, H. Zhang, *Appl. Catal. A* 466 (2013) 300–306.
- [18] H. Li, J. Ren, X. Qin, Z. Qin, J. Lin, Z. Li, *RSC Adv.* 5 (2015) 96504–96517.
- [19] S. Takenaka, T. Shimizu, K. Otsuka, *Int. J. Hydrogen Energy* 29 (2004) 1065–1073.
- [20] J. Kopyscinski, T.J. Schildhauer, S.M.A. Biollaz, *Fuel* 89 (2010) 1763–1783.
- [21] X. Lin, L. Lin, K. Huang, X. Chen, W. Dai, X. Fu, *Appl. Catal. B* 168–169 (2015) 416–422.
- [22] Y. Zeng, H. Ma, H. Zhang, W. Ying, D. Fang, *Fuel* 137 (2014) 155–163.
- [23] Y. Wang, R. Wu, Y. Zhao, *Catal. Today* 158 (2010) 470–474.
- [24] J. Ren, Z. Li, S. Liu, Y. Xing, K. Xie, *Catal. Lett.* 124 (2008) 185–194.
- [25] C. Guo, Y. Wu, H. Qin, J. Zhang, *Fuel Process Technol.* 124 (2014) 61–69.
- [26] S. Takenaka, *Int. J. Hydrogen Energy* 29 (2004) 1065–1073.
- [27] S. Takenaka, H. Ogihara, I. Yamanaka, K. Otsuka, *Appl. Catal. A* 217 (2001) 101–110.
- [28] S. Takenaka, H. Ogihara, K. Otsuka, *J. Catal.* 208 (2002) 54–63.
- [29] S. Tang, L. Ji, J. Lin, H. Zeng, K. Tan, K. Li, *J. Catal.* 194 (2000) 424–430.
- [30] L. Ji, S. Tang, H.C. Zeng, J. Lin, K.L. Tan, *Appl. Catal. A* 207 (2001) 247–255.
- [31] C.H. Bartholomew, *Appl. Catal. A* 212 (2001) 17–60.
- [32] K.P. De Jong, J.W. Geus, *Catal. Rev.* 42 (2000) 481–510.
- [33] K. Takehira, T. Ohi, T. Shishido, T. Kawabata, K. Takaki, *Appl. Catal. A* 283 (2005) 137–145.
- [34] J. Zhang, H. Wang, A. Dalai, *J. Catal.* 249 (2007) 300–310.
- [35] K. Takanabe, K. Nagaoka, K. Narai, K. Aika, *J. Catal.* 232 (2005) 268–275.
- [36] S.K. Pal, J. Jiang, E.I. Meletis, *Surf. Coat. Technol.* 201 (2007) 7917–7923.
- [37] Z. Zhang, X. Verykios, *Catal. Today* 21 (1994) 589–595.
- [38] J. Guo, H. Lou, X. Zheng, *Carbon* 45 (2007) 1314–1321.
- [39] J. Zhang, H. Wang, A.K. Dalai, *J. Catal.* 249 (2007) 300–310.
- [40] A. Kambolis, T.J. Schildhauer, O. Kröcher, *CHIMIA Int. J. Chem.* 69 (2015) 608–613.
- [41] C. Sheng, *Fuel* 86 (2007) 2316–2324.
- [42] X. Guo, J. Ren, C. Xie, J. Lin, Z. Li, *Energy Convers. Manage.* 100 (2015) 45–55.
- [43] M.B.I. Chowdhury, M.M. Hossain, P.A. Charpentier, *Appl. Catal. A* 405 (2011) 84–92.
- [44] J. Ren, S. Liu, Z. Li, K. Xie, *Catal. Commun.* 12 (2011) 357–361.
- [45] B. Xu, C. Sievers, S. Hong, R. Prins, J. Vanbokhoven, *J. Catal.* 244 (2006) 163–168.